

# International Journal of Applied Mathematics in Control Engineering

Journal homepage: <http://www.ijamce.com>

## Design of Control System for Water Quality Monitor in Irrigating Farmland

Ying Wang, Yao Gou, Qi Liu\*, Baohua Li, Shuo Li, Kai Liang

*Jilin Institute of Chemical Technology, Chengde Street, Jilin, 132000, China*

### ARTICLE INFO

Article history:

Received 20 April 2018

Accepted 20 July 2018

Available online 25 December 2018

Keywords:

Single-chip computer;

Irrigation agriculture water quality;

flow control system; stability;

high precision

### ABSTRACT

This paper designed the driving control circuit of flow injection module based on single chip microcomputer technology, for agricultural irrigation water quality monitor flow sampling control system with high stability and high precision requirements, introduced the driving circuit of peristaltic pump and a number of valve control circuit, and performed a test for the circuit control accuracy. The experimental results showed that the design based on single chip microcomputer control circuit could improve the water quality monitor flow sampling circuit stability and the accuracy of the flow injection, laid the key technical basis for irrigation water quality monitor to improve the reliability.

Published by Y.X.Union. All rights reserved.

## 1. Introduction

Water pollution has become one of the important factors that affect agricultural production. If water quality can be monitored in real time, and water pollution can be found and treated, this is for agricultural production. The development of an advanced online water quality monitoring system has important practical significance and huge market demand<sup>[1]</sup>. Most of the irrigation water quality monitoring instruments get the test results by comparing the standard curve between the target liquid and the standard liquid, so the precision of the instrument flow sampling module directly affects the accuracy of the water quality test results, accurate and stable sampling is very important. In order to improve the stability of the instrument and the accuracy of water quality detection, this paper studies the control circuit of the sampling module of the irrigation water quality monitor<sup>[2]</sup>.

## 2. Flow system design of irrigation water quality monitor

The overall structure of the irrigation water quality monitor system designed in this paper is shown in figure 1. The embedded control system adopts Linux operating system and the processor adopts ARM microprocessor. The embedded control system selects different reagent paths by controlling multiple valves, and then controls the peristaltic pump to pump a certain amount of reagent into the test chamber to accelerate the reagent reaction by stirring<sup>[3]</sup>. The light emitted by the light source is absorbed by the liquid in the detection chamber and received by the micro spectrometer through

the light path. Then the micro-spectrometer transmits the absorbance data to the embedded control system through the serial port.

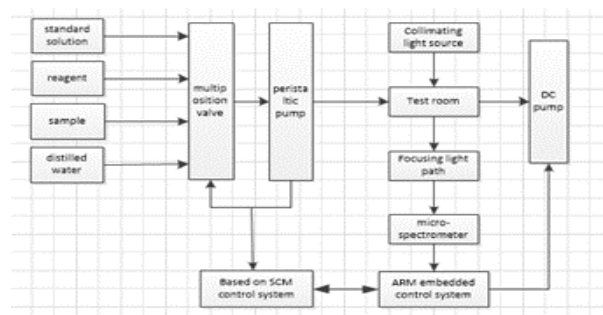


Fig. 1. General structure of irrigation agriculture water quality monitor system

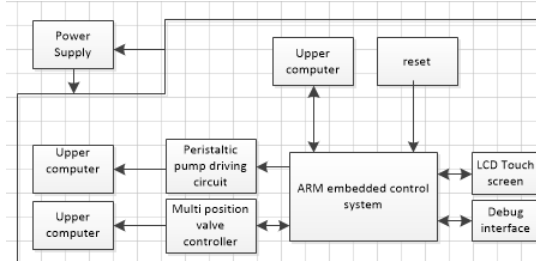


Fig.2. Circuit diagram of the system design for water quality monitor

The embedded control system determines the concentration of a component of the solution to be measured by comparing the absorbance of the solution to the standard solution absorbance and

\* Corresponding author.

E-mail addresses: [liuqi20002@sina.com](mailto:liuqi20002@sina.com) (Q. Liu)

concentration standard curve, so as to realize the rapid real-time monitoring of water quality parameters<sup>[4]</sup>.

2.1 Overall circuit design block diagram

The overall circuit system design diagram of the water quality monitor is shown in figure 2. This circuit takes the ARM microprocessor as the control core, and the peripheral circuit includes rich interfaces, which theoretically can well coordinate and stabilize the control system. ARM microprocessor peripheral circuit includes complex<sup>[5]</sup>. Bit circuit, LCD display circuit, touch screen circuit, serial port circuit used for communication with upper computer and some other debugging interfaces. The drive and control circuit of flow device mainly includes the serial control circuit of multi-valve and the drive and control circuit of peristaltic pump. The driving control circuit of several valves and peristaltic pump is the key content of this design and is also the important content directly related to the work effect of the sample injection module<sup>[6]</sup>.

2.2 Power supply circuit

In this paper, 24V dc power supply is adopted as the power supply of the system<sup>[7]</sup>. The 24V dc power supply can directly offer power to multiple valves, which is also the highest voltage required in the flow system. The drive circuit of peristaltic pump needs 12V and 5V as power supply, while the USB interface circuit and LCD display circuit need 5V as power supply. Figure 3 shows the power supply circuit designed according to the typical application circuit of the LM2596 switch voltage regulator with a fixed output of 12V. Capacitance C33 is an aluminum electrolytic capacitor of 220 F. As a by-pass capacitor, it is used to prevent large transient voltage at the input end and maintain the stability of dc input voltage<sup>[8]</sup>. The Schottky diode 1N5824 and inductance L1 are combined as the circuit's continuative diode to ensure the voltage stability and prevent the device from burning. Capacitor C34 adopts tantalum capacitance of 220 F as the compensation capacitance of output end to guarantee the stability of output voltage<sup>[9]</sup>.

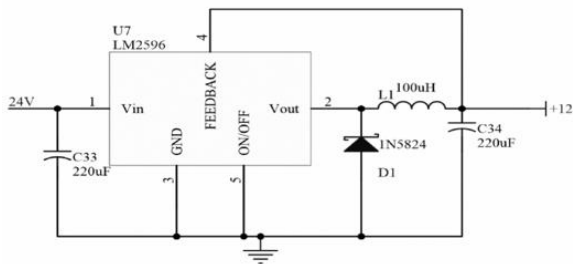


Fig.3. Principle diagram of 12V power supply circuit

3. ARM microprocessor peripheral circuit

The ARM microprocessor used in this paper is Samsung's S3C2410 chip. For this design, S3C2410 has an LCD controller, which provides 1 channel LCD dedicated DMA, 3 channel UART (Universal asynchronous transceiver), 8 channel 10-bit ADC and touch screen interface, and 2 port USB (universal serial bus) host / 1 port USB devices<sup>[10]</sup>.

3.1 Numerical parameters

The J12 pin of ARM microprocessor is the n RESET pin. To reset the microprocessor, a low level of at least four clock cycles must be added to the n RESET pin. In the circuit, STC811T chip is used as

the generation chip of RESET signal. When there is a jump from low to high level on the chip's MR pin, the RESET pin will produce a low level lasting 200 S. As shown in figure 4, when the button SW1 is not pressed, the MR pin remains at high level. When the button is pressed, the MR pin changes to a low level. When the button is released, the level recovers to a high level. At this time, a jump from low to high level is completed. The RESET pin is connected to the J12 n RESET pin of the microprocessor, and the low-level time of 200 S ensures the microprocessor RESET<sup>[11]</sup>.

3.1 LCD touch screen circuit

The circuit design of the touch screen is shown in figure 5. In the circuit, two FDC6321 chips, namely four MOS tubes, are used to realize the switch control of the pin level of touch screen. The resistance R16 and capacitance C24, R17 and C25 in the circuit diagram constitute two low-pass filters, which are used to filter out high frequency noise of Y coordinate signal and X coordinate signal respectively<sup>[12]</sup>.

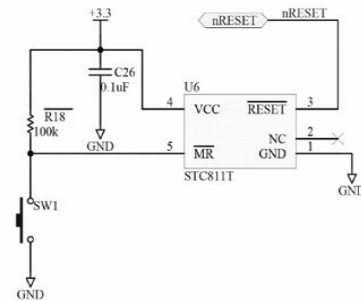


Fig.4. Reset circuit

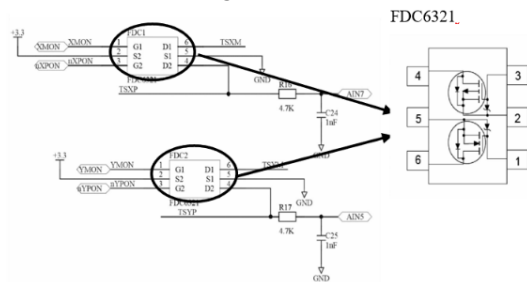


Fig.5. Control circuit of the touch screen

DNS have been performed for  $Re=180$  and  $400$  (Reynolds number based on wall-shear velocity  $u_\tau$  and channel half-height  $H$ ) in a periodic channel of streamwise and spanwise size  $L_x/H = 4.0$  and  $L_z/H = 4.0$ , where  $2H$  is the distance between the plane walls. Two-dimensional and three dimensional ripples have been placed on virtual surface near the lower wall, which is shown in Fig. 1.

4. Flow injection control circuit

4.1 Micro step motor peristaltic pump driving circuit

The micro-stepping motor peristaltic pump is driven by the two-phase micro-stepping motor drive circuit. The circuit diagram of the creep pump driving circuit is shown in figure 6. The upper part of the circuit is the control signal processing circuit, and the lower half is the stepper motor drive circuit. In order to enable the signal, EN controls whether the drive circuit works or not<sup>[13]</sup>. The step signal is the pulse signal required for the step motor. Because the output voltage of the ARM chip pin is 3.3 V and the driving

capacity is limited, the 3.3V power supply is connected in the circuit, and the transistor 9013 is used as the switch. The control signal controls the conduction of the subsequent circuit by controlling the base voltage of the transistor<sup>[14]</sup>.

In order to reduce the mutual interference between the control circuit and the drive circuit, the front and rear end of the circuit is isolated by using the controllable photocoupler TLP521. In order to ensure the signal quality, the optocoupler output is connected to the 4HC14D six-bit reverse Schmitt flip-flop. After 74HC14D shaping, the simulation results of the circuit are shown in figure 7. The real line in the diagram is the signal waveform after the inverse Schmitt flip-flop. The dashed line is the output signal after the light coupling. From the diagram, we can see that the waveform of the signal will be greatly improved<sup>[15]</sup>.

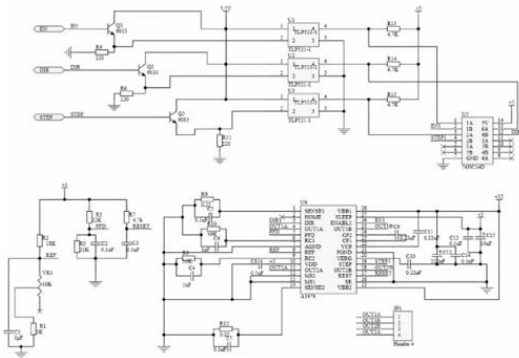


Fig.6. Drive circuit of the peristaltic pump

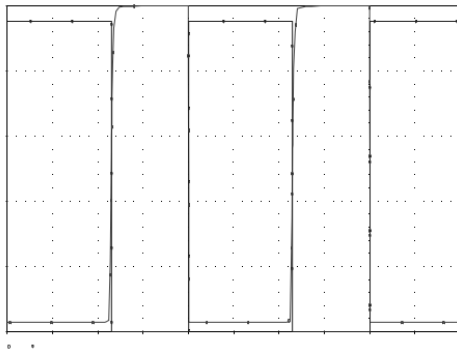


Fig.7. Simulation results of control signal processing circuit

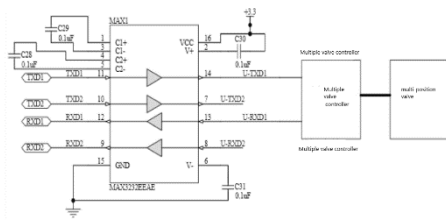


Fig.8. Communication circuit of multiposition valve ports

4.2 Multi-valve control circuit

The multi-position valve self-contained control module used in the flow path sampling module can communicate with the upper computer through the serial port. The level of serial port communication is 5V, and that of ARM microprocessor is 3.3V. so it is necessary to match the serial port of micro-processing S3C2410 with the serial port of multi-bit valve module by means of serial port conversion chip MAX3232. The ARM chip can complete the control of the multi-bit valve by sending the corresponding

instruction to the control module of the multi-bit valve through the serial port. The multi-bit valve serial communication circuit is shown in figure 8.

5. Materials and methods

4.1 Defining the problem

We tried to use the Extreme Learning Machine algorithm to solve the analysis problem of design of control system that are not easy to judge reliability.

The machine-learning based single-frame SR is developed for the proposed contact-imaging.

4.2 Establish a database

The database used in this study was derived from a database of 20 years of operation of a factory in a variety of industries using SCM as the main control software.

4.3 Modeling

According to the data we need, we can build a reliability analysis model based on deep learning algorithm. The output of this model should be consistent with our task objectives. By analyzing the data in the database and its weight, we define the following functions:

$$C_{on} = f(D_{obj}) = \frac{A}{1 + \left(\frac{D_{obj}}{D}\right)^B} \quad (1)$$

where A is the contrast amplitude, D is the characteristic distance, and B is the shape parameter. Guided by (1), we first discuss the design of microfluidic channel and then CMOS image sensor.

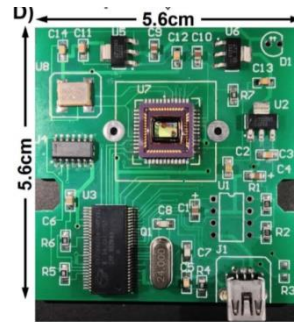


Fig.9. Forming drawing of pcb

Next, the CMOS image sensor chip was soldered on one lowcost 5.6 cm ×65.6 cm printed circuit board (PCB) that provides the sensor with power supplies and digital control signals as shown in Fig.9. The data transferred from the CMOS image sensor to PC was through a USB interface (CY7C68013-56 EZ-USB FX2, San Jose, CA), which ensures high-speed imaging with maximum data transfer rates of 56 Mbytes per second. The sensor working status such as exposure time, ROI and number of frames to capture was controlled by the status registers that can be accessed through a two-wire serial interface, i.e., SCLK and SDATA. They are set through the custom designed GUI. We set 6406480 image ROI of the sensor to capture the flowing specimens at a sensor frame rate of ,200 frames/s (fps)<sup>[16]</sup>.

In the experiments, the microfluidic chip was connected to a syringe pump (KDS Legato180, Holliston, MA) through silastic laboratory tubing and samples were pumped into the microfluidic

chamber continuously at a typical flow rate of ,5 mL/min under the illumination from a white light source (Olympus LG-PS2, Tokyo, Japan). The light source was placed 12 cm above the sensor and the light intensity at the sensor surface was 1.5 k Lux. The exposure time of the sensor was set 75  $\mu$ s, corresponding to 3 rows of sensor readout time. The readout LR frames were buffered with digital image processing conducted to improve the resolution by single-frame ELM-SR processing. As such, the developed system can automatically recognize and count<sup>[17]</sup>.

The ELM-SR includes off-line training and on-line testing. In the training step, a reference model is trained that can map the interpolated LR images with the HF components extracted from the HR images from the training library.

In the off-line training step, given the input of HR image  $HR_{M \times N}$ , where  $M$  is the row pixel number and  $N$  is the column pixel number, a corresponding LR image  $LR_{M \times N}$  is first generated through bicubic down sampling. Note that the down sampling factor is the same as the SR enhancement factor  $t$ , i.e.,  $M=m \times t$ ,  $N=n \times t$ . Next, the generated LR image  $LR_{M \times N}$  is interpolated back to  $LR\_Int'_{M \times N}$ , which has the same size of  $HR_{M \times N}$  but blurred and lack of HF component details. As such, by subtracting the HR image  $HR_{M \times N}$  with the interpolated LR image  $LR\_Int'_{M \times N}$ , the HF component  $HF_{M \times N}$  is obtained, i.e.,

$$HF_{M \times N} = HR_{M \times N} - LR_{M \times N} \quad (2)$$

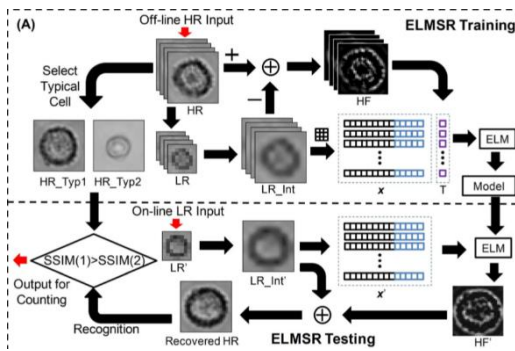


Fig.10. ELM-SR Training A

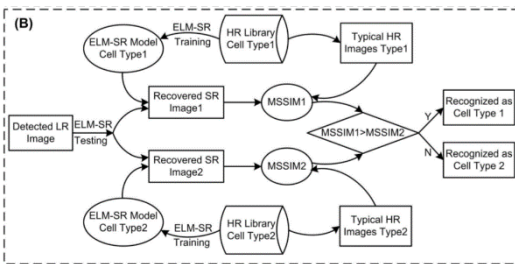


Fig.10. ELM-SR Training B

Based on  $p$  HF images  $HF_{M \times N}$  from the training library, the training targeting value  $T$  is obtained which is a  $p \cdot MN \times 1$  row vector of all the pixels intensity values in HF images. Meanwhile, the pixel intensity pattern existed in  $LR\_Int'_{M \times N}$  is extracted by a 363 pixel patch  $P(i, j)$  centered at pixel  $(i, j)$  of  $LR\_Int'_{M \times N}$  to search through the whole image, where  $1 \ll j \ll M - 1$  and  $1 \ll j \ll N - 1$ . As such, the column vectors extracted from all patches in  $p$  interpolated images  $LR\_Int'_{M \times N}$  compose the feature matrix  $X$ . Thus, the ELM training dataset  $(X, T)$  is generated.

As such, ELM can take the input  $(X, T)$  to ELM to calculate a

row vector  $\beta$  containing the weights by

$$T = \beta G(AX + B) \quad (3)$$

where  $G$  is a sigmoid function, and  $A$  and  $B$  are randomly generated matrix. The training data with  $A$ ,  $B$  and  $\beta$  can be used for the ELM-SR reference model in figure 10 and in figure 11.

In the on-line testing step, when a detected LR cell image  $LR_{M \times N}$  is inputted, the corresponding SR image can be recovered using the same  $A$ ,  $B$  and the trained  $b$  as follows. The resolution of  $LR_{M \times N}$  is first enhanced by  $t$  times through bicubic interpolation to  $LR\_Int'_{M \times N}$ . The same patch searching method used in the ELM-SR training is applied to extract the feature matrix  $X'$  from  $LR\_Int'_{M \times N}$ . Thus, one can calculate the row vector  $T'$  that includes the recovered HF components  $HF'_{M \times N}$  for the input LR image  $LR_{M \times N}$ . As such, the final SR image  $SR'_{M \times N}$  is recovered with the sufficient HF details for cell type recognition by

$$SR'_{M \times N} = HF'_{M \times N} + LR\_Int'_{M \times N} \quad (4)$$

when a detected LR cell  $LR'_{M \times N}$  is inputted, two SR images,  $SR1'_{M \times N}$  and  $SR2'_{M \times N}$  can be recovered, each corresponding to one reference model. Afterwards,  $SR1'_{M \times N}$  and  $SR2'_{M \times N}$  are compared with the typical HR images  $HR1_{M \times N}$  and  $HR2_{M \times N}$  in the training libraries, where the mean structural similarity (MSSIM/SSIM) index is employed to characterize the similarity<sup>[18]</sup>. The SSIM is a full reference metric between 0 and 1 to indicate the similarity between one SR image with one distortion free reference HR image by

$$SSIM(SR, HR) = \frac{(2\mu_{SR}\mu_{HR})(2\sigma_{SR,HR})}{(\mu_{SR}^2 + \mu_{HR}^2)(\sigma_{SR}^2 + \sigma_{HR}^2)} \quad (5)$$

where  $\mu_{SR}$  and  $\mu_{HR}$  are the means of the SR and HR images,  $\sigma_{SR}^2$  and  $\sigma_{HR}^2$  are the variances of the SR and HR images, and  $\sigma_{SR,HR}$  is the covariance of the SR and HR images. It is proven to be consistent with human eye perception compared with traditional metric such as peak signal-to-noise ratio (PSNR) and mean squared error (MSE). The MSSIM is the average of the SSIMs for one SR image with all the typical HR images

$$MSSIM(SR, HRlib) = \frac{1}{K} \sum_{k=1}^K SSIM(SR, HR_k) \quad (6)$$

where  $K$  is the number of typical HR images in the HR training library. For  $SR1'_{M \times N}$  and  $SR2'_{M \times N}$ , MSSIM1 and MSSIM2 can be calculated. Then we categorize the cell to the type that has the stronger MSSIM.

As such, with the ELM-based single-frame SR processing, the developed microfluidic machine can have much better imaging capability to distinguish in the continuously flowing microfluidic<sup>[19]</sup>.

#### 4.4 Model performance evaluation

With the use of extreme learning machine for single-frame super-resolution processing, one prototype of contact-imaging based microfluidic monitor is demonstrated for recognition and counting. The developed system resolves the resolution limitation of contact imaging by on-line image recognition based super-resolution processing, which enables continuous high throughput flowing cell recognition and counting. The developed system is validated with comparison to the commercial flow monitor<sup>[20]</sup>.

Mobile robot technology involves many research fields and has been widely used in all walks of life, representing the frontier of high technology. Mobile robots can obtain environmental information and their own state, in the presence of obstacles in the environment to complete specific tasks. At present, when solving path planning problems in complex environments, conventional algorithms have many defects, such as poor robustness and low efficiency, but rough set theory and genetic algorithm (GA) are a new type of intelligent optimization algorithm, with strong robustness, implicit parallelism, global optimization performance, and easy to sum up with other algorithms. The algorithm based on rough set theory and genetic algorithm provides a reasonable basis for the research of path planning of mobile robot<sup>[21]</sup>.

Search space: mainly refers to the possible state, position and direction of the robot.

Initial state and target state: this is how the robot moves from the initial state to the target state.

Constraints: the "optimal" plan is primarily concerned with time, distance, safety, invisibility, and energy consumption constraints for the robot.

Algorithm: analyze the relevant conditions of path planning, and apply the relevant algorithm to the path planning.

Action: a path plan refers to the method from the starting point to the target point.

Time: "at time t the robot will move to the point (x, y) or" consume the shortest time. "Time is simply expressed as A series of actions:" after action A is completed, the robot starts action B".

Planning: the sequence of actions from the start point to the target point<sup>[22]</sup>.

There are many considerations in path planning that will affect the design and judgment criteria of the system:

Environment: what does path planning adequately represent in the environment? Is the application space indoor or outdoor? Is it messy or relatively open?

Space and time complexity: is it fast enough that the robot doesn't have to stop and think?

Dynamic or unknown: path planning can process information or change targets.

Optimization: requirements are based on the shortest distance, time, media security, etc.

Integrity: does it find an optimal path to exist?

The work plan or path planning algorithm in motion can be divided into three general decomposition methods:

Cytolysis: the distinction between free and restrained cells.

Roadmap: determine a group of routes in free space.

Potential field: the space in which a mathematical function is implemented<sup>[23]</sup>.

The potential field has the limitation that the target robot is stuck outside the local minimum. This defect has been overcome in potential field research.

The potential field is often referred to as a local method rather than a global method, because the impact in the robot field is almost entirely based on nearby obstacles. Obstacles do not affect the movement of the robot, so it cannot be a useful planning method. There is a simpler and more efficient way to use potential field method for path planning.

PRM usually USES secondary barriers based on other roadmap plans rather than gradual consumption. This means that obstacles require a well-defined outline and generate variable path costs that are more difficult than other approaches. When obstacles are added

or removed from the map, the entire roadmap must be regenerated. Because first-generation roadmaps are slow to complete in time, planning functions are poor when information changes frequently or the original information is incorrect. Figure 3 shows the "sparse area" and "dense area" coverage of PRM.

Assuming that A is an m×n order matrix, where all the elements belong to the real number domain or the complex number domain K, singular value decomposition of matrix A is carried out: where U is an m×m order unitary matrix; D is a semi-positive definitem × ndiagonal matrix; and V conjugate transpose  $V^T$  is an n×n unitary matrix. That's the singular value decomposition of A. D diagonal element  $D_i$ , where i is the singular value of A

$$A = UDVT$$

In the above expression,  $D = \text{diag}(\sigma_1, \sigma_2, \dots, \sigma_q)$  and  $\sigma_1 \geq \sigma_2 \geq \dots \geq \sigma_q, q > 0$ .

Define singular value:

$$E = \sum_{i=1}^q \sigma_i^2 \tag{7}$$

Then, define the range difference and normality of singular values as shown below:

$$P(i) = \frac{\sigma_i^2 - \sigma_{i+1}^2}{E} \tag{8}$$

$$f(x) = \sin\left(\frac{2\pi x f_1}{f_s}\right) + \frac{2x f_2}{f_s} + u_i(x) \tag{9}$$

U is a constant, and the formula is expressed as follows:

$$\frac{\partial C}{\partial t} = D_L \frac{\partial^2 C}{\partial x^2} - u \frac{\partial C}{\partial x} \tag{9}$$

$$C(x, t)|_{t=0} = 0, 0 \leq x < +\infty$$

$$C(x, t)|_{x=0} = C_0, t > 0 \tag{10}$$

$$C(x, t)|_{x \rightarrow +\infty} = 0, t > 0$$

After Laplace changes, the formula of standard normal distribution function is as follows:

$$C = 1 - \Phi_{0.1} \left[ \frac{x - ut}{\sqrt{2D_L t}} \right] \tag{11}$$

$$I_T^2 = U_T^2 / R^2 = \frac{4KT \Delta f}{R} \tag{12}$$

$$U_T = \sqrt{4KTR_1 \Delta f_e} \tag{13}$$

To solve the problem of path optimization, the model predictive control is called  $X_t$ , which can be expressed by K gaussian equation such as equation (14) and (15):

$$P(Xt) = \sum w_i, t \times \eta(Xt, \mu_i, t, \sum_i, t) \tag{14}$$

$$\eta(Xt, \mu i, t, \sum i, t) = \frac{e^{-\frac{1}{2}(Xt - \mu i, t)^T \sum_{i,j}^{-1} (Xt - \mu i, t)}}{(2\pi)^{\frac{n}{2}} \left| \sum i, t \right|^{\frac{1}{2}}} \quad (15)$$

Through the combination of robust speed control and disturbance model, under the condition of constant output disturbance, is defined as:

$$y_1(t) = y(t) - \phi_1^T(t)\theta, \quad (16)$$

A feasible solution can be obtained to predict the steady-state optimization problem. The equation is shown in (17)-(19) :

$$wi, t = (1 - \alpha) \times wi, t - 1 + \alpha \quad (17)$$

$$\mu i, t = (1 - \rho) \times \mu i, t - 1 + \rho \times Xt \quad (18)$$

$$\sigma_{i,t}^2 = (1 - \rho) \times \sigma_{i,t-1}^2 + \rho(Xt, \mu i, t - 1)^T \times (Xt - \mu i, t - 1) \quad (19)$$

Considering the delay,  $L$  can be expressed as:

$$L^0 = \begin{bmatrix} C_{ijkl}^0 & e_{kij}^0 \\ e_{ikl}^{0T} & -\eta_{ik}^0 \end{bmatrix} \quad (20)$$

These functions can be expressed as follows:

$$\begin{aligned} C(x) &= C^0 + C^1(x) \\ e(x) &= e^0 + e^1(x) \end{aligned} \quad (21)$$

$$\begin{aligned} \eta(x) &= \eta_0 + \eta_1(x) \\ \rho(x) &= \rho_0 + \rho_1(x) \end{aligned} \quad (22)$$

The difference between superscript 1 and superscript 1 is as follows:

$$\begin{aligned} C^1 &= C - C^0, e^1 = e - e^0 \\ \eta^1 &= \eta - \eta^0, p^1 = p - p^0 \end{aligned} \quad (23)$$

The integral equation of the whole function can be simplified into the following form:

$$\begin{aligned} f(x, \omega) &= f^0(x, \omega) + \int_v S(x - x') (L^1 F(y')) \\ &+ \rho_1 \omega^2 g(R) T_1 f(y') S(y') dy' \end{aligned} \quad (24)$$

$F(t)$  is defined as:

$$\left[ \frac{\partial}{\partial t} + \varepsilon \right]^2 f(t) = \delta(t) \quad (25)$$

$$\begin{aligned} \bar{g}(k, t) &= \frac{1}{2\pi} \int_{-\infty}^{+\infty} \frac{e^{-i\omega t}}{k^2 + \left( \varepsilon - i \frac{\omega}{c} \right)^2} d\omega \\ &= c^2 \Theta(t) \frac{\sin(ckt)}{ck} e^{-\varepsilon t} \end{aligned} \quad (26)$$

Based on the research of path planning of mobile robot, an optimization algorithm combining rough set theory and genetic

algorithm is proposed. The second step is to find the global optimal path by combining rough set theory and genetic algorithm. The simulation results show that the proposed method has strong dynamic convergence and is optimized compared with other mobile robot global path planning algorithms<sup>[24]</sup>.

In this paper, the viewable method is mainly used for environmental modeling to show the influence of ground environment modeling on braking distance path extension<sup>[25]</sup>. Combined with the method of combining rough set theory and genetic algorithm, an intelligent optimization method is used for the path planning and development of mobile robots. The simulation results show that the proposed method has strong dynamic convergence and is optimized compared with other mobile robot global path planning algorithms.

## 6. Analysis of experimental results

The hardware circuit is debugged by modules. After the debugging is correct, the flow sampling precision test platform is set up and the precision test is carried out to verify the stability and accuracy of the circuit. According to the target monitored by the irrigation water quality monitor and the requirements of the test project, the sample volume required to be determined in the experiment includes 0.2ml, 0.8ml, 1.0ml, 1.2ml, 2.0ml and 2.5ml. In order to ensure the precision of sample injection and facilitate the experiment, distilled water with a density of 0.9999 g/mL was used as the target reagent. The mass of reagent extracted from peristaltic pump is weighed by high precision electronic balance and its volume is obtained.

Frequency times	Volume of reagent taken by the peristaltic pump at sampling					
	A1	A5	A10	A15	A20	A26
1	1.9952	0.7946	0.2015	1.0052	1.1855	2.4985
2	1.9947	0.8065	0.1964	0.9895	1.2086	2.5004
3	1.9911	0.7996	0.2002	1.0100	1.1898	2.4978
4	2.0003	0.7913	0.2008	0.9941	1.2001	2.4973
5	1.9994	0.8127	0.2021	0.9983	1.1994	2.4974
Mean value	1.9962	0.8009	0.2002	0.9994	1.1967	2.4983
repeat	99.6%	99.1%	99.8%	99.2%	99.1%	99.9%

Fig.10. Test data of sampling precision

All the results recorded in the test are the best sampling results after the step adjustment of stepping motor. The experimental data of injection accuracy test is shown in figure 10. From the test data in figure 9, it can be calculated that the absolute value of the relative error between the measured value and the theoretical value is less than 2%. The flow-way injection precision is very high, which meets the design requirements<sup>[26]</sup>. The error relative to the mean value presents standard randomness, the variance is less than 0.0001, and the measurement precision is very high. Relative standard deviation is about 1%, and the flow control system has good reproducibility.

## 7. Conclusion

The development of advanced irrigation water quality monitoring system has important practical significance for the development of modern agriculture. In order to improve the stability and accuracy of the sampling module, the flow path sampling control circuit of the irrigation water quality monitor is designed by using the single-chip microcomputer control system. The experimental results show that the absolute value of the relative error between the measured value and the theoretical value is less than 2%, the variance is less than 0.0001, the sampling precision and the measuring precision of the flow path are very high, and the flow

path control system has good reproducibility.

## References

- [1] Tang X, Li H J, Chen Y T, et al. Research on Multi-Task Control Model of PLC[J]. *Advanced Materials Research*, 2014, 889-890:1236-1239.
- [2] Liao B, Yu J, Zhang T, et al. Energy-efficient algorithms for distributed storage system based on block storage structure reconfiguration[J]. *Journal of Network & Computer Applications*, 2013, 48(1):71-86.
- [3] Shen X B. The Unified Model of Computer Architectures[J]. *Chinese Journal of Computers*, 2007: 5729-5736
- [4] Hermenegildo M. Automatic parallelization of irregular and pointer-based computations: Perspectives from logic and constraint programming[M]// *Euro-Par'97 Parallel Processing*. Springer Berlin Heidelberg, 1997:31-45.
- [5] Xiong X M, Zhang W X. The Study of Reliability Design on PLC Control System[J]. *Colliery Mechanical & Electrical Technology*, 2004(3):13-16
- [6] Li H J, Yan J J, Yan L, et al. Application of Man-Machine Isolation Automation Assembly for Industrial Electric Detonator[J]. *Applied Mechanics & Materials*, 2014, 716-717:1522-1526.
- [7] Huang, Guang Bin, Q. Y. Zhu, and C. K. Siew. Extreme learning machine: a new learning scheme of feedforward neural networks. *IEEE International Joint Conference on Neural Networks*, 2004. *Proceedings IEEE*, 2005(2): 985-990
- [8] LUO, X., GE, S., WANG, J. & GUAN. Time Delay Estimation-based Adaptive Sliding-Mode Control for Nonholonomic Mobile Robots. *International Journal of Applied Mathematics in Control Engineering*, 2018, 1, 1-8
- [9] DU, W., ZHAO, X., DU, H. & LV, F. Fault Diagnosis of Analog Circuit based on Extreme Learning Machine. *International Journal of Applied Mathematics in Control Engineering*, 2018, 1, 9-14.
- [10] WEI, W., LIANG, B. & ZUO, M. Linear Active Disturbance Rejection Control for Nanopositioning System. *International Journal of Applied Mathematics in Control Engineering*, 2018, 1, 92-95.
- [11] LIU, H., LV, X. & XIAO, J. The Research Status and Prospect of Particle Swarm Optimization Algorithm for Water Environment Quality Assessment. *International Journal of Applied Mathematics in Control Engineering*, 2018, 1, 23-30.
- [12] ZHAO, T. & WANG, J. Multimodal Transport Path Planning based on Multilateration (MLAT) System Using a Pulse Neural Network Model. *International Journal of Applied Mathematics in Control Engineering*, 2018,1, 55-61.
- [13] SUGIUCHI Hajime, YONESHIMA Jun, KOHAMA Satoshi. Development of control system for small humanoid robot [C]. *The Proceedings of JSME annual Conference on Robotics and Mechatronics (Robomec)*, 2017.
- [14] TAGE Atsushi, KUSAKABE Yasuhito, IKEURA Ryojun, HAYAKAWA Soichiro. Impedance Control of a Series Elastic System with a Torque Controlled Actuator[C]. *The Proceedings of JSME annual Conference on Robotics and Mechatronics (Robomec)*, 2017.
- [15] WU, W. J. Parametric Lyapunov Equation Approach to Stabilization and Set Invariance Conditions of Linear Systems with Input Saturation. *International Journal of Applied Mathematics in Control Engineering*, 2018, 1, 79-84
- [16] PENG, R., CHENG, L., DAI, Y., ZHAO, X., WU, H. & CHEN, Y. Design and Implementation of Monocular Vision SLAM for Mobile Robot Based on ROS. *International Journal of Applied Mathematics in Control Engineering*, 2018,1, 85-91.
- [17] MENG, R. 2018. Adaptive Parameter Estimation for Multivariable Nonlinear CARMA Systems. *International Journal of Applied Mathematics in Control Engineering*, 1, 96-102.
- [18] SHI, S., LIU, M. & MA, J. Fractional-Order Sliding Mode Control for a Class of Nonlinear Systems via Nonlinear Disturbance Observer. *International Journal of Applied Mathematics in Control Engineering*, 2018, 1, 103-110.
- [19] Rui-Dong Wang, Xue-Shan Sun, Xin Yang, Haiju Hu. Cloud Computing and Extreme Learning Machine for a Distributed Energy Consumption Forecasting in Equipment-Manufacturing Enterprises[J]. *Cybernetics and Information Technologies*, 2016,16(6):83-97.
- [20] S. Shi, Liu M., and Ma J., Fractional-Order Sliding Mode Control for a Class of Nonlinear Systems via Nonlinear Disturbance Observer. *International Journal of Applied Mathematics in Control Engineering*, 2018. 1(1):103-110.
- [21] J. Tan, The Mechanical Meaning of Bernstein Basis Function. *International Journal of Applied Mathematics in Control Engineering*, 2018. 1(1):47-54.
- [22] W. Wei, Liang B., and Zuo M., Linear Active Disturbance Rejection Control for Nanopositioning System. *International Journal of Applied Mathematics in Control Engineering*, 2018. 1(1): 92-95.
- [23] Hai-Jun Rong, Rong-Jing Bao, Guang-She Zhao. Model Reference Adaptive Neural Control for nonlinear systems based on Back-Propagation and Extreme Learning Machine[P]. *Intelligent Sensors, Sensor Networks and Information Processing (ISSNIP)*, 2014 IEEE Ninth International Conference on, 2014.
- [24] Chaimae Elhatri, Mohammed Tahifa, Jaouad Boumhidi. Extreme Learning Machine-Based Traffic Incidents Detection with Domain Adaptation Transfer Learning[J]. *Journal of Intelligent Systems*, 2017, 26(4): 601-612.
- [25] Lei Yu, Danning Zhao, Hongbing Cai. Extreme Learning Machine for the Predictions of Length of Day[J]. *Artificial Satellites*, 2015, 50(1)19-33.



**Wang Ying** is currently teaching at Jilin College of chemical engineering. In 2003, she obtained the bachelor's degree of Jilin University. In 2008, she received her master's degree from Dalian university of technology. Her main research interests are artificial intelligence, intelligent robots, Measurement and control technology. Jilin college of chemical engineering associate professor.

**Gou Yao** is currently studying for Postgraduate Degree in Jilin Institute of Chemical Engineering. In 2017 he completed his bachelor's degree in Si Chuan University mainly engaged in robot.



currently studying for Degree in Jilin Institute of Engineering In 2017 he bachelor's degree in Si Jin Jiang College. He is the direction of intelligence



**Liu Qi** is currently teaching at Jilin Institute of Chemical Engineering. In 2003, he obtained the bachelor's degree of Jilin University. In 2008, he received my master's degree from Dalian university of technology. His main research interests are artificial intelligence, industrial robots and industrial automation control. He is an associate professor at Jilin Institute of Chemical Engineering.



**Li Baohua** is currently studying for Postgraduate Degree in Jilin Institute of Chemical Engineering. In 2017, he completed his bachelor's degree in Jilin Institute of Chemical Engineering. He is mainly engaged in the direction of industrial robots.



**Li Shuo** is currently studying for Postgraduate Degree in Jilin Institute of Chemical Engineering. In 2017, he completed his bachelor's degree in Jilin Institute of Chemical Engineering. He is mainly engaged in the direction of industrial robots.



**Liang Kai** is currently studying for Postgraduate Degree in Jilin Institute of Chemical Engineering. In 2017, He completed his bachelor's degree in City college of hebei university of technology. Mainly engaged in mobile robot navigation technology, road strength planning and advanced algorithm research.

